THE CATHOLIC UNIVERSITY OF AMERICA
DEPARTMENT OF ELECTRICAL ENGINEERING

FINAL REPORT

on

A STUDY OF SPACE-RATED CONNECTORS USING A ROBOT END-EFFECTOR

Research Grant NAG 5-1415

Dr. Charles C. Nguyen
Principal Investigator and Professor

submitted to
Mr. Lloyd Purves
Code 714 Goddard Space Flight Center (NASA)
Greenbelt, Maryland

April 1995

Contents

REPORT SUMMARY

This is a final report presenting the research results obtained from a research grant entitled "A Study of Space-Rated Connectors Using a Robotic End-Effector," funded by the Goddard Space Flight Center (GSFC/NASA) with a Grant Number NAG 5-1415, for the period from August 15, 1990 to December 31, 1994. The main research activities of the above research grant have been directed toward the study of the Robot Operated Materials Processing System (ROMPS), developed at GSFC under a flight project to investigate commercially promising in-space material processes and to design reflyable robot automated systems to be used in the above processes for low-cost operations. The research activities can be divided into two phases. Phase I dealt with testing of ROMPS robot mechanical interfaces and compliant device using a Stewart Platform testbed and Phase II with computer simulation study of the ROMPS robot control system. This report provides a summary of the results obtained in Phase I and Phase II.

1 Introduction

The Robot Operated Materials Processing System (ROMPS) has been developed at Goddard Space Flight Center (GSFC) under a flight project to investigate commercially promising in-space material processes and to design reflyable robot automated systems to be used in the above processes for low-cost operations [3]. The ROMPS completed its first flight in 1994 as a Hitchhiker payload in a Get Away Special (GAS) can. An important component of the ROMPS is a three degree-of-freedom (DOF) robot which has been responsible for carrying out the required tasks of in-space processing of selected materials.

This is a final report which presents the research results obtained from a study of the ROMPS robot under a research grant entitled "A Study of Space-Rated Connectors Using a Robotic End-Effector," funded by the Goddard Space Flight Center (GSFC/NASA) with a Grant Number NAG 5-1415, for the period from August 15, 1990 to December 31, 1994. The ROMPS study was divided into two phases. Phase I concentrated on testing of ROMPS robot mechanical interfaces and compliant device using a Stewart Platform testbed while Phase II studied the performance of the ROMPS robot control system using computer simulation. In this report, we will summarize the results obtained in Phase I and Phase II.

2 Phase I: Testing of ROMPS Robot Components

2.1 The ROMPS Robot

Figure 1.1 gives a sketch of the ROMPS designed to fit within a full-size GAS can. As seen from the figure, the ROMPS basically consists of a robot possessing three DOFs located in the center of the ROMPS, 148 pallets located around the robot on six racks and two ovens located at the top. A simplified version of Figure 1.1 is presented in Figure 1.2 which illustrates the ROMPS robot, a rack containing several pallets and the two ovens. Using Figure 1.2, the steps required in the operation of the ROMPS robot are described as follows:

1. The robot moves to a rack and use its fingers to acquire a pallet containing a sample of material
2. The robot moves to an oven and places the pallet under it
3. The oven heats up the sample while the robot is holding it
4. The robot moves a storage rack and replaces the sample in the rack
5. The robot repeats Steps 1-4 until all samples are processed or a stop command is issued

Based on the description of the above steps, we identify the following tasks the robot must carry out in each particular step:

1. Step 1 requires a successful mating between the robot fingers and the pallet interface
2. Step 2 requires a successful insertion of two pins of the oven into the two holes of the pallet
3. Step 3 requires a successful insertion of the pallet into the rack and a successful demating between the robot fingers and the pallet interface

In the tasks described above, misalignments between the fingers and the pallet interface (Step 1), between the pallet holes and the oven pins (Step 2) and between the pallet interface and the rack (Step 3) may exist because of imperfectness in manufacturing of the parts or errors in the robot position controllers and sensors. A passive compliant device which is composed of two orthogonal nested double blade flexures as shown in Figure 1.4 is mounted between the robot wrist and robot fingers to provide compliance in the radial and elevation (vertical) directions and thereby to help the fingers to accommodate the misalignments. Under unforeseen misalignments, a task (mating, insertion or demating) is called *successful* if it can be completed within the working range of the passive compliant device in terms of allowable travel and forces and without any damages to the parts involved.

2.2 Study Objective and Test Plan

2.2.1 Study Objective

The main objective of this study is to experimentally evaluate the effectiveness of the passive compliant device in accommodating misalignments and to evaluate the design of the robot fingers, the pallet interface, the oven holes and the rack based on their mating and/or insertion capability.

2.2.2 Test Plan

In order to achieve the study objective, a test plan is prepared to aim at three different scenarios:

- **Scenario 1: The Pallet/Finger Test**
- **Scenario 2: The Pallet/Oven Test**
- **Scenario 3: The Pallet/Rack Test**

In each of the above scenarios, the following tasks will be carried out:

1. **Operation Under Perfect Alignment:** Check for operation under perfect alignment
2. **Determination of Capture Ranges:** Using visual inspection, determine the capture ranges
3. **Operation under Misalignments:** Perform mating (insertion)/demating under carefully introduced misalignments, measure and record applied forces/torques in six DOFs

2.3 The Testbed and Test Setup

The testbed employed in this study is depicted in Figure 1.3. The desired misalignments are produced by a Stewart Platform-based (SPB) manipulator possessing six DOF's [2]. The manipulator mainly consists of a lower base platform, an upper payload platform, and six linear actuators. The movable payload platform is supported above the stationary base platform by the linear actuators which are composed of ballnuts and ballscrews providing the extensibility. Stepper motors were selected to drive the ballscrews to extend or shorten the actuator lengths whose variations will in turn produce the motion of the payload platform. The manipulator specifications are given below:

- Tracking accuracy of 1/1000 inch
- Maximum endpoint velocity of 3.2 inches per second

- A six DOF working envelope of one cubic foot
- Payload capacity of 2000 lbs

The test setup is illustrated in Figure 1.4 and Figure 1.5. The robot finger assembly is mounted to a stationary location using a vice and the pallet is mounted to the upper payload platform of the SPB manipulator via the passive compliant device as shown in Figure 1.4. Forces/torques exerted during the mating between the fingers and the pallet interface are measured by a six DOF JR3 force/torque sensor mounted between the compliant device and the upper manipulator platform. Coordinate transformation is used to transform measured forces/torques to forces/torques at the center of the passive compliant device.

We now refer to Figure 1.5 (test setup for Scenario 1) and Figure 1.6 to explain the coordinate systems. Assuming that the pallet has been brought to a pose aligned with the ROMPS robot fingers as seen in Figure 1.5, relationship between the coordinate system used by the SPB manipulator and the ROMPS coordinate system is illustrated in Figure 1.6. We observe that the elevation axis of the ROMPS robot (indicated by z_{ROMPS}) lies in the opposite direction of the y-axis of the SPB manipulator (indicated by y_M) and the radial axis of the ROMPS robot lies in the opposite direction of the x-axis of the SPB manipulator (indicated by x_M). The ROMPS robot azimuth axis coincides with the negative rotation around the y_M-axis of the SPB manipulator. Thus a desired misalignment between the pallet interface and the fingers can be produced by rotating and/or translating the upper manipulator platform using the coordinate systems shown in Figure 1.6. In particular, in order to produce a misalignment of +0.5 inch in the ROMPS elevation direction, the upper manipulator platform should move -0.5 inch in the y_M axis. As shown in Figure 1.5, although the test setup is intended for Scenario 1, the oven pins or the rack can be mounted in the same position of the finger assembly for Scenarios 2 or Scenario 3, respectively, as illustrated in Figure 1.7.

2.4 Test Procedures and Results

2.4.1 Scenario 1: The Pallet/Finger Test

- **Perfect Alignment Operation:** Referring to Figure 1.5, we now describe the testing procedures for Scenario 1. First the perfect alignment between the ROMPS robot fingers and the pallet was established by controlling the SPB manipulator to move the pallet into a position which is roughly aligned with the fingers. The fingers were then commanded to grasp on the pallet interface. After that, the SPB manipulator was controlled to slowly and carefully modify its pose until the reading of forces/torques measured by the JR3 sensor was zero. The pose of the pallet relative to the fingers at which no forces/torques are applied is the perfect alignment pose. Finally the fingers were commanded to open (demating) and then close (mating) under the perfect alignment. According to force reading, the forces/torques exerted to the compliant device were negligible during the mating and mating of the fingers with the pallet interface.
- **Capture Range Determination:** The capture ranges for the Finger/Pallet grasping were not visually determined. However they will be determined in Section 2.6 (to be presented later) using the results obtained from the test for operation under misalignments presented below.
- **Operation under Misalignments:** From the above-established perfect alignment pose, the SPB manipulator was controlled to translate and/or rotate to produce the amount of desired misalignment (in inches or degrees) in a selected axis. Then the fingers were controlled to grasp the pallet interface. The force/torques in the misalignment axes were measured and are now tabulated in Tables 1 and 2 given below. Table 1 shows results for translational misalignments in x_M-axis and y_M-axis while Table 2 the results for rotational misalignments about the x_M-axis y_M-axis and z_M-axis.

x_M-axis[in.]	F_{x_M}[lb.]	y_M-axis[in.]	F_{y_M}[lb.]
-0.1	2.3	-0.1	2.0
-0.15	4.1	-0.15	3.2
-0.2	5.2	-0.2	3.7
-0.25	7.4	-0.25	5.3
-0.3	19.7	-0.3	5.7
0.1	-2.8	0.1	-2.4
0.15	-4.0	0.15	-3.5
0.2	-5.5	0.2	-4.1
0.25	-7.6	0.25	-5.2
0.3	-18.8	0.3	-5.9

Table 1 Translation misalignments in x_M and y_M axes

x_M-axis[deg]	T_{x_M}[lb-in]	y_M-axis[deg]	T_{y_M}[lb-in]	z_M-axis[deg]	T_{z_M}[lb-in]
-0.5	28	-0.5	153	-0.5	4
-1.0	60	-1.0	298	-1.0	7
-1.5	100	0.5	-170	-1.5	15
-2.0	138	1.0	-324	-2.0	25
0.5	-20			0.5	-8.5
1.0	-39			1.0	-12
1.5	-70			1.5	-21
2.0	-103			2.0	-32

Table 2 Rotational misalignments about x_M, y_M and z_M axes

2.4.2 Scenario 2: The Pallet/Oven Test

The Pallet/Oven test was performed with the oven assembly containing the two pins mounted to a stationary position using a vice and the pallet assembly mounted to the upper platform of the SPB manipulator via the JR3 force/torque sensor.

- **Perfect Alignment Operation:** First the perfect alignment between the oven pins and the pallet was established by controlling the SPB manipulator to move the pallet into a position above the open pins so that the holes on the pallet roughly aligned with the pins. Then the SPB manipulator was controlled to push the pallet onto the pins. After that, the SPB manipulator was controlled to slowly and carefully modify its pose until the reading of forces/torques measured by the JR3 sensor was zero. The resulting pose at which no forces/torques were read was the perfect alignment pose. At the end, the SPB manipulator was controlled to move out from the perfect alignment pose. From the resulting pose, to evaluate the operation under perfect alignment, the SPB manipulator was controlled to move the pallet holes onto the oven pins then demate the pallet from the oven. According to force reading, there were no noticeable forces/torques exerted to the compliant device during the mating and demating.

- **Capture Range Determination:** The capture ranges for the oven/pallet were determined using the following procedures. First the SPB manipulator was controlled to move out from the perfect alignment about 1 in. Then from the resulting pose, the SPB manipulator was used to introduce

single-axis misalignments, one axis at a time. After the misalignment was introduced, the pallet was controlled to move onto the oven pins and the gap between the oven surface and the pallet surface was inspected. The misalignments were increased in small increments and after each increase, the above process was repeated. The capture range for each axis was determined as the misalignment amount just before the surfaces of the oven and the pallet failed to completely flush. In other words, any misalignment which is smaller or equal to the capture range ensures the complete flushedness of the surfaces. In each of the misalignment cases, an 0.15 in. overtravel was commanded in the involved axis to help the passive compliant device to make the two surfaces to flush. The capture ranges for the oven/pallet test are tabulated in Table 3 given below. As shown in Table 3, the capture range for translation in x_M-axis was found to be ± 0.15 in. However, the oven pins and pallet holes were designed so that the oven surface and the pallet surface flush completely under a misalignment of ± 0.25 in. along the x_M-axis. As a result, the pallet holes and the oven pins were re-designed and manufactured. Testing of the new setup showed that the capture range for the x_M-axis is ± 0.20 in.

translation along x_M-axis	rotation about x_M-axis	rotation about y_M-axis	rotation about z_M-axis
± 0.150 *inches*	± 0.5 *degrees*	± 6.0 *degrees*	± 1.0 *degrees*

Table 3 Capture ranges for Scenario 2, Pallet/Oven

- **Operation under Misalignments:** Using the same procedure as discussed above, mating between the oven pins and the pallet holes under single-axis misalignments was investigated. In particular, for each of the misalignments to be studied, after the misalignment was introduced, the oven pins were mated and then demated with the pallet holes. During the mating and demating, forces/torques in six DOFs at the center of the passive compliant device were measured and recorded.

  For the old Pallet/Oven, the following work was carried out:

  1. **Translational Misalignment along x_M-axis:** Forces (torques) along (about) x_M-axis, y_M-axis and z_M-axis were measured for mating under perfect alignment, and under misalignments of 0.05 in., 0.1 in., 0.15 in., 0.2 in., -0.05 in, -0.1 in., -0.15 in., and -0.2 in. along x_M-axis.
  2. **Rotational Misalignment about x_M-axis:** Forces (torques) along (about) x_M-axis, y_M-axis and z_M-axis were measured for mating under misalignments of 0.5 deg., 1.0 deg., 1.5 deg., 2.0 deg., -0.5 deg., -1.0 deg., -1.5 deg., and -2.0 deg. about x_M-axis.
  3. **Rotational Misalignment about y_M-axis:** Forces (torques) along (about) x_M-axis, y_M-axis and z_M-axis were measured for mating under misalignments of 0.5 deg., 1.0 deg., -0.5 deg., and -1.0 deg. about y_M-axis.
  4. **Rotational Misalignment about z_M-axis:** Forces (torques) along (about) x_M-axis, y_M-axis and z_M-axis were measured for mating under misalignments of 0.5 deg., 1.0 deg., 1.5 deg., 2.0 deg., -0.5 deg., -1.0 deg., -1.5 deg., and -2.0 deg. about z_M-axis.

  For the new Pallet/Oven, the following work was completed:

  1. **Translational Misalignment along x_M-axis:** Forces (torques) along (about) x_M-axis, y_M-axis and z_M-axis were measured for mating under perfect alignment, and under misalignments of 0.05 in., 0.1 in., 0.15 in., 0.2 in., -0.05 in, -0.1 in., -0.15 in., and -0.2 in. along x_M-axis.

2.5 Scenario 3: The Pallet/Rack Test

The Pallet/Rack test was conducted with the rack mounted to a stationary position using a vice and the pallet assembly mounted to the upper platform of the SPB manipulator via the JR3 force/torque sensor. Two different racks were considered, a rack marked with a letter on it S, which is referred hereto as the *S Rack* and a rack with high tolerance, which is referred hereto as the *High Tolerance Rack*.

- **Perfect Alignment Operation:** The perfect alignment pose was established using the same procedures of the other scenarios. First the SPB manipulator was controlled to move the pallet into a position roughly aligned with the rack. Then the pallet was carefully pushed into the rack. After that, the SPB manipulator was controlled to slowly and carefully modify its pose until the it reached a pose at which the reading of forces/torques measured by the JR3 sensor was zero. This pose was the perfect alignment pose. Finally from the perfect alignment pose, the pallet was moved out of the rack. To evaluate the operation under perfect alignment, from the above resulting pose, the SPB manipulator was controlled to insert the pallet into the rack and again demate the pallet from the rack. Six DOF forces/torques exerted during the insertion and demating were measured and recorded. The above process was done for both the S Rack and the High Tolerance Rack. According to force reading, there were no noticeable forces/torques exerted during the insertion and demating for both racks.

- **Capture Range Determination:** The capture ranges for the rack/pallet were visually determined and presented in Table 4 given below:

	translation along y_M-axis [in.]	rotation about x_M-axis [deg.]	rotation about y_M-axis [deg.]	rotation about z_M-axis [deg.]
S Rack	-0.3	±7.0	±8.0	±8.0
High Tolerance Rack	-0.3	±7.0	±8.0	±8.0

Table 4 Capture ranges for Scenario 3, Pallet/Rack

- **Operation under Misalignments:** Using the same procedure employed in other scenarios, insertion of the pallet into the rack under single-axis misalignments was investigated.

  For the S Rack, the following tests were performed:

  1. **Translational Misalignment along y_M-axis:** Forces (torques) along (about) x_M-axis, y_M-axis and z_M-axis were measured for insertion under perfect alignment, and under misalignments of 0.05 in., 0.1 in., 0.15 in., 0.2 in., 0.25 in., 0.30 in., -0.05 in, -0.1 in., -0.15 in., -0.2 in., -0.25 in, and -0.30 in. along y_M-axis.
  2. **Rotational Misalignment about x_M-axis:** Forces (torques) along (about) x_M-axis, y_M-axis and z_M-axis were measured for mating under misalignments of 0.5 deg., 1.0 deg., 1.5 deg., 2.0 deg., -0.5 deg., -1.0 deg., -1.5 deg., and -2.0 deg. about x_M-axis.
  3. **Rotational Misalignment about y_M-axis:** Forces (torques) along (about) x_M-axis, y_M-axis and z_M-axis were measured for mating under misalignments of 0.5 deg., 1.0 deg., 1.5 deg., 2.0 deg., -0.5 deg., -1.0 deg., -1.5 deg., and -2.0 deg. about y_M-axis.
  4. **Rotational Misalignment about z_M-axis:** Forces (torques) along (about) x_M-axis, y_M-axis and z_M-axis were measured for mating under misalignments of 0.5 deg., 1.0 deg., 1.5 deg., 2.0 deg., -0.5 deg., -1.0 deg., -1.5 deg., and -2.0 deg. about z_M-axis.

For the High Tolerance Rack, the following tests were finished:

1. **Translational Misalignment along y_M-axis:** Forces (torques) along (about) x_M-axis, y_M-axis and z_M-axis were measured for insertion under perfect alignment, and under misalignments of 0.05 in., 0.1 in., 0.15 in., 0.2 in., 0.25 in., 0.30 in., -0.05 in, -0.1 in., -0.15 in., -0.2 in., -0.25 in, and -0.30 in. along y_M-axis.
2. **Rotational Misalignment about x_M-axis:** Forces (torques) along (about) x_M-axis, y_M-axis and z_M-axis were measured for mating under misalignments of 0.5 deg., 1.0 deg., 1.5 deg., 2.0 deg., -0.5 deg., -1.0 deg., -1.5 deg., and -2.0 deg. about x_M-axis.
3. **Rotational Misalignment about y_M-axis:** Forces (torques) along (about) x_M-axis, y_M-axis and z_M-axis were measured for mating under misalignments of 0.5 deg., 1.0 deg., -0.5 deg., and -1.0 deg. about y_M-axis.
4. **Rotational Misalignment about z_M-axis:** Forces (torques) along (about) x_M-axis, y_M-axis and z_M-axis were measured for mating under misalignments of 0.5 deg., 1.0 deg., 1.5 deg., 2.0 deg., -0.5 deg., -1.0 deg., -1.5 deg., and -2.0 deg. about z_M-axis.

2.6 Discussions of Results of Phase I

This section gives comments, observations and evaluations which are based upon the experimental results obtained from the tests.

1. **Operation under Perfect Alignment:** Based upon obtained test results, we found that operation under perfect alignment including mating (grasping, insertion) and demating for all three scenarios, Pallet/Finger, Pallet/Oven and Pallet/Rack has been successful. This has been derived from the fact that no noticeable forces/torques were exerted to the compliant device during the mating and demating under perfect alignment for all scenarios.
2. **Operation under Misalignment:** From experimental results, we find, as expected, that the magnitudes of forces/torques exerted in an axis are proportional to the amount of misalignment in this axis. The proportionality is however nonlinear.
3. **Capture Ranges for Pallet/Finger:** The capture ranges were not determined for the Finger/Pallet test. However using Table 1, from the fact that the maximum force that the compliant device can yield in the radial and elevation axes is 10 lb., we can safely state that the capture ranges for x_M-axis and y_M-axis are ± 0.25 in. and ± 0.30 in., respectively since the forces in the respective axis did not exceed 10 lb.
4. **Improvement of Pallet/Oven:**
   - After finding out that the old Pallet/Oven does not meet the specification, the old oven pins were re-manufactured (based on George Veollmer's suggestions) to have longer taper, larger diameter and longer length. In addition, the pallet holes were re-manufactured to accommodate the new oven pins.
   - As stated earlier, the capture range of the Pallet/Oven in the radial-axis of the compliant device was increased from ± 0.15 in. (old Pallet/Oven) to ± 0.20 in. (new Pallet/Oven).
   - From the results, we find that the new Pallet/Oven has substantial improvement in force time responses. Inspection of other cases of misalignment reveals that the forces are generally decreased if the new Pallet/Oven was used.
5. **Compliant Device Performance:**

- After conducting the tests presented in this report, we found that the compliant mechanism performed according to its specifications. Based upon the test results, the compliant device provided large compliance in the radial and elevation axes and small compliance in other axes. In addition, it has been able to accommodate misalignments up to $\pm$ 0.2 in. in all the compliance axes (radial and elevation) without exceeding the maximum allowed force of 10 lb. and without hitting the mechanical stops in all three scenarios.
- Inspecting the time histories of forces/torques for the Pallet/Oven and Pallet/Rack scenarios, we note that the compliant device has good damping which is manifested by generally smooth transitions from mating (insertion) to demating or vice versa without any significant surges in forces/torques.
- From Table 1, we conclude that the compliant device possesses symmetry in the compliance axes, namely the radial and elevation axes and non-symmetry in other axes.

3 Phase II: Study of ROMPS Robot Control System

3.1 Description of the ROMPS Robot Axes

The ROMPS side view is illustrated in Figure 2.2 showing the three axes of the ROMPS robot and its gripper. The axes are driven by brushless DC motors manufactured by Inland Motor Company. The elevation axis utilizes a roller screw to provide the elevation DOF defined as the vertical motion of the gripper. A rotary encoder is mounted on the motor shaft for elevation measurement. The azimuth DOF defined as the rotation about the elevation axis utilizes a rotary encoder mounted on the motor shaft and a 160:1 harmonic drive. The radial DOF defined as the *in-and-out* motion of the gripper is realized by an 1 mm lead ball screw and a linear encoder for displacement measurement. The gripper assembly mainly consists of two fingers equipped with Hall effect sensors and an Inland brushless motor driving a 50:1 harmonic drive with 1/4-16 acme screw. The assembly is mounted to the radial axis screw via a compliant device that provides passive compliance along the radial and elevation axes. As explained above the three DOFs and the gripper will enable the ROMPS robot to move the gripper to the vertical position of a pallet using the elevation and azimuth DOFs, to slide the gripper fingers into the pallet rack using the radial DOF and then to grasp the pallet using the gripper fingers. The radial DOF will then enable the robot to slide the pallet out of the rack. The robot will then use the elevation and radial DOFs to take the pallet to a desired rack and place it there using the radial axis and the opening of the gripper fingers. Thus it is important to study the position control system to be used to control the axes and the gripper so that their gains can be set properly in order to ensure a successful mission of the ROMPS.

3.2 Study Cases

The four cases to be studied in this report are described below:

- **Study Case 1: Single Axis Motions in Free Space**
  This case investigates the decoupled motion of each single axis in free space. Each axis will be ramped up to maximum speed and ramped down to stop at a desired position. The controller gains will be adjusted until the position trajectory tracks the desired one within given accuracy specifications without overshoot and oscillations. In this case, reasonable steady velocity errors are acceptable. Observation will be made to find out if the acceleration and deceleration of the axes will excite the wrist compliant device enough to cause the gripper to oscillate. Consequently the spring mass model of the gripper and the compliant device will be derived to monitor possible oscillations during the acceleration and deceleration periods so that we can determine whether or not the compliant device bang against its hard stops.
- **Study Case 2: Compliant Motion of the Elevation Axis**
  The target position of the furnace to which the grasped pallet must be brought to may be shifted

during launch or because of manufacturing error. If the target elevation is reduced, then the wrist compliant device can be used to compensate for the position error. It is also desired for the gripper to make a good contact with the furnace bottom by applying a specified contact force via the compliant device. This case studies the ability of the position control scheme of the elevation axis in reaching a target position and in applying a specified contact force in a compliant motion mode generated by the wrist compliant device. As illustrated in Figure 2.3, the elevation axis will be commanded to a position 1/8th of an inch past the location at which the gripper impacts the furnace bottom so that the compliant device is loaded to approximately 5 lb. It will be observed if oscillations occur at the time of impact. If oscillations occur, then we will determine if reduction in approaching velocity can help minimizing impact forces and oscillations.

- **Study Case 3: Radial Axis Motion under Resistance**
  This case studies the motion the radial axis performs in pulling out a pallet held in a rack under detent springs as illustrated in Figure 2.4. The radial axis will be commanded to pull out to free space. The pallet will initially resist the motion due to detent spring forces, then will break free and slides out under friction force against the rack. Observation will be made whether or not the control scheme is capable of overcoming the initial detent spring forces. The detent spring force will be modeled as a 5 lb threshold to break loose from the detents.

- **Study Case 4: Compliant Motion of the Gripper Finger**
  This case investigates the ability of the gripper fingers to grasp a solid object under a specified contact force. To do so, the gripper will be commanded to close on a solid object to a position 1/4th of an inch past the position at which the fingers first make contact with the object so that the gripper compliance device is loaded to about 10 lb. The control scheme for the gripper will be evaluated in terms of position and contact force accuracy.

3.3 Modeling of the ROMPS Robot

This section is devoted to developing the modeling equations for the ROMPS robot. First it shows the similarity and relationship between a general permanent magnet (PM) DC motor and the brushless DC motor used in the ROMPS robot. Modeling equations for a PM DC motor are then presented. After that, the overall transfer function matrices for PIR and PR controllers will be derived, respectively, and these transfer functions will be used in next section to determine the controller gains which ensure the system stability. Then vibrations caused by the wrist compliant device along the elevation and radial axes will be modeled using spring-mass systems. Finally motor load torque generated by pushing the gripper against the furnace bottom (Study case 3) will be modeled and computed.

3.3.1 Brushless DC Motor and PM DC Motor

The variables and parameters used for motors are first defined below:

$i_a(t)$	: armature current	L	: armature inductance
R	: armature resistance	$e_a(t)$	: armature voltage
$e_b(t)$	: back emf	K_b	: back-emf constant
$T_L(t)$	: load torque	$\omega_m(t)$	: rotor angular velocity
$T_m(t)$	: motor torque	J_m	: rotor inertia of motor
$\theta_m(t)$	: rotor displacement	B_m	: viscous-friction coefficient
$K_t(t)$	: torque constant	n	: number of poles
T_f	: maximum inertia torque (static friction and cogging torque)		

The motors used in the ROMPS robot are all brushless DC motors manufactured by the Inland Motor Company. After several discussions with an engineer of Inland Motor Company, it is concluded that the

following equations describe the dynamic characteristics of a brushless motor:

$$e_a(t) = i_a\ R + \omega_m(t)\ K_b + L\ \frac{di_a}{dt} \tag{1}$$

$$L\ \frac{di_a}{dt} = L\ \frac{n}{\pi}\ i_a(t)\ \omega_m(t) \tag{2}$$

and

$$i_a(t) = \frac{T_L + T_f + B_m\omega_m(t)}{K_t} \tag{3}$$

On the other hand, a PM DC motor can be modeled by: [1]

$$e_a(t) = R\ i_a(t) + e_b(t) + L\ \frac{di_a}{dt} \tag{4}$$

$$T_m(t) = K_t\ i_a(t) \tag{5}$$

$$e_b(t) = K_b\ \omega_m(t) \tag{6}$$

and

$$T_m(t) = J_m\frac{d^2\theta_m(t)}{dt^2} + T_L(t) + B_m\frac{d\theta_m(t)}{dt} \tag{7}$$

Investigating Equations (3)-(7), we conclude that Equation (1) is equivalent to Equation (4) and Equation (3) is equivalent to Equation (7). In particular, we note that

$$T_f = J_m\frac{d^2\theta_m(t)}{dt^2} \tag{8}$$

Since we just show that the modeling equations for the brushless DC motor and PM DC motor are equivalent, from now on we use the modeling equations of PM DC motor to model the brushless motor.

3.3.2 State Equation Representation of PM DC motor

From Equations (4) - (7), the state representation of a PM DC motor is obtained as follows:

$$\dot{\mathbf{x}}(t) = \mathbf{A}\mathbf{x}(t) + \mathbf{B}\mathbf{u}(t) \tag{9}$$

$$\mathbf{y}(t) = \mathbf{C}\mathbf{x}(t) \tag{10}$$

where

$\mathbf{x}(t) = \left[\ i_a(t) \quad \omega_m(t) \quad \theta_m(t)\ \right]^T$ = state vector

$\mathbf{u}(t) = \left[\ e_a(t) \quad T_L(t)\ \right]^T$ = input vector

$\mathbf{y}(t) = \theta_m(t)$ = output

and

$$\mathbf{A} = \begin{bmatrix} -\frac{R}{L} & -\frac{K_b}{L} & 0 \\ \frac{K_t}{J_m} & -\frac{B_m}{J_m} & 0 \\ 0 & 1 & 0 \end{bmatrix},\ \mathbf{B} = \begin{bmatrix} \frac{1}{L} & 0 \\ 0 & -\frac{1}{J_m} \\ 0 & 0 \end{bmatrix},\ \mathbf{C} = \begin{bmatrix} 0 & 0 & 1 \end{bmatrix} \tag{11}$$

The output $\mathbf{y}(t)$ and the input vector $\mathbf{u}(t)$ are related by

$$\mathbf{Y}(s) = \mathbf{G}(s)\mathbf{U}(s) \tag{12}$$

where $\mathbf{Y}(s)$ and $\mathbf{U}(s)$ denote the Laplace transform of $\mathbf{y}(t)$ and $\mathbf{u}(t)$, respectively. $\mathbf{G}(s)$ is called the transfer function matrix which can be determined as: [1]

$$\mathbf{G}(s) = \mathbf{C}(s\mathbf{I} - \mathbf{A})^{-1}\mathbf{B} = \begin{bmatrix} \frac{K_t}{\Delta_1(s)} & -\frac{R+Ls}{\Delta_1(s)} \end{bmatrix} \tag{13}$$

where

$$\Delta_1(S) = LJ_m s^3 + (RJ_m + LB_m)s^2 + (B_m R + K_t K_b)s \tag{14}$$

Using Equations (9)-(14), the DC motor can be represented in a block diagram as shown in Figure 2.5.

3.3.3 The Overall Transfer Function Matrix

Figure 2.6 illustrates the control system of the brushless DC motor. The control scheme consists of a proportional (P) controller, a switched integral (I) controller and a rate-feedback (R) controller. Rate-feedback controller is selected instead of derivative controller because of the improvement of the system damping. In the following, the overall transfer function matrices for the ramping period in which the I controller is *off* and for the steady-state period in which the I controller is *on* will be derived.

- **Case 1: PIR Controller (Steady-State Period)**

  The following development assumes that the integral controller is switched "on". From Equations (12) and (13), we obtain

  $$\Theta(s) = \frac{K_t}{\Delta_1(s)} E_a(s) - \frac{R + Ls}{\Delta_1(s)} T_L(s) \tag{15}$$

  From Figure 2.6, $E_a(s)$ can be computed as

  $$E_a(s) = [U_1(s) - K_f \Theta(s)] (K_P + \frac{K_I}{s}) - K_R K_f s \Theta(s) \tag{16}$$

  where K_P, K_I and K_R denote gain matrices of the proportional, integral and rate controllers, respectively, and K_f is the roller screw constant. Substituting Equation (16) into (15) and solving for $\Theta(s)$, we obtain

  $$\Theta(s) = \frac{(K_t K_P s + K_t K_I) U_1(s) - (Ls^2 + Rs) T_L(s)}{\Delta_2(s)} \tag{17}$$

  where

  $$\Delta_2(s) = s\Delta_1(s) + K_t K_R K_f s^2 + K_t K_f K_P s + K_t K_f K_I \tag{18}$$

  From Equation (17), we can write

  $$\Theta(s) = T_{PIR}(s) \begin{bmatrix} U_1(s) & T_L(s) \end{bmatrix}^T \tag{19}$$

  where the overall transfer function matrix $T_{PIR}(s)$ is given by

  $$T_{PIR}(s) = \begin{bmatrix} \frac{K_t K_P s + K_t K_I}{\Delta_2(s)} & -\frac{Ls^2 + Rs}{\Delta_2(s)} \end{bmatrix} \tag{20}$$

- **Case 2: PR Controller (Ramping Period)**

  In this case, we assume that the integral controller is switched "off" and the overall transfer function is derived as follows:

  For $K_I = 0$, $E_a(s)$ in Equation (16) becomes

  $$E_a(s) = [U_1(s) - K_f \Theta(s)] K_P - K_R K_f s \Theta(s) \tag{21}$$

Substituting Equation (21) into (15) and solving for $\Theta(s)$, we have

$$\Theta(s) = \frac{K_t K_P U_1(s) - (Ls + R)T_L(s)}{\Delta_3(s)} \tag{22}$$

where

$$\Delta_3(s) = \Delta_1(s) + K_t K_R K_f s + K_t K_f K_P \tag{23}$$

From Equation (22), we obtain

$$\Theta(s) = T_{PR}(s) \begin{bmatrix} U_1(s) & T_L(s) \end{bmatrix}^T \tag{24}$$

where the overall transfer function matrix $T_{PR}(s)$ is given by

$$T_{PR}(s) = \begin{bmatrix} \frac{K_t K_P}{\Delta_3(s)} & -\frac{Ls+R}{\Delta_3(s)} \end{bmatrix} \tag{25}$$

3.3.4 Vibration Modeling

This section derives equations to model the gripper vibrations caused by the wrist compliant device. Vibrations can occur along the elevation axis and radial axis. The dynamics of the gripper assembly along the elevation axis can be modeled by a spring-mass system as illustrated in Figure 2.7.

Using Newton's second law, the equation of motion for the model in Figure 2.7 is obtained as

$$m_e(a_m + a_e) = -k_e x_1 \tag{26}$$

where

a_e : acceleration of the radial axis with respect to the robot base
a_m: acceleration of the gripper assembly with respect to the radial axis along the elevation axis
m_e: equivalent mass of the gripper assembly along the elevation axis
k_e : equivalent spring constant of the wrist compliant device along the elevation axis

In (26) replacing a_m by $\ddot{x_1}$ where x_1 denotes the displacement of the gripper assembly with respect to the radial axis yields

$$m_e\ddot{x_1} + k_e x_1 + m_e a_e = 0 \tag{27}$$

The dynamics of the gripper assembly along the radial axis is modeled by another spring-mass system as shown in Figure 2.8. Applying the same approach as in the case of elevation axis, the equation of motion for the radial axis is derived as

$$m_r\ddot{x_2} + k_r x_2 + m_r a_r = 0 \tag{28}$$

where

a_r : acceleration of the radial axis with respect to the base of the radial axis motor
a_m: acceleration of the gripper assembly with respect to the radial axis along the radial axis
m_r: equivalent mass of the gripper assembly along the radial axis
k_r : equivalent spring contant of the wrist compliant device along the radial axis

In the computer simulation to be conducted later, a_e and a_r in (27) and (28), respectively can be computed from Equation (7).

3.3.5 Modeling of the Motor Load Torque

This section is devoted to modeling and computing the motor load torque generated by the wrist compliant device when the robot gripper is pushed against the furnace bottom (Study Case 2) as illustrated in Figure 2.9. If the elevation axis is commanded to a position which is Δx bigger than the position at which the gripper makes the first contact with the furnace bottom, then the resulting elastic force generated by the wrist compliant device is transmitted to the elevation axis motor as a load torque. The load is computed by

$$T_L = K_f \; F_C = K_f \; k_e \Delta x \tag{29}$$

where F_C is the elastic force generated by the wrist compliant device along the elevation axis and K_f is the roller screw constant of the elevation axis.

Similar to Study Case 2, Study Case 4 requires the modeling and computation of the load torque generated by the gripper compliance spring when the gripper fingers are commanded to close on a solid object to a position which is Δx greater than the contact position. Using the same approach applied for the above case, the load torque transmitted to the gripper axis motor is computed by

$$T_L = K_f \; k_g \; \Delta x \tag{30}$$

where K_f denotes the ACME screw constant of the gripper axis and k_g, the spring constant of the compliance mechanism of the gripper fingers.

3.4 Stability Analysis

This section utilizes the Routh Hurwitz criterion to determine the controller gains which ensure the system stability. It comprises two parts. The first part deals with the PIR controller for steady-state period while the second part, the PR controller for ramping period.

- **Case 1: PIR Controller**

  The Routh array of $\Delta_2(s)$ for the PIR controller is given as follows:

s^4	LJ_m	$RB_m + K_t K_b + K_t K_f K_R$	$K_t K_f K_I$
s^3	$LB_m + J_m R$	$K_t K_f K_P$	
s^2	W_1	$K_t K_f K_I$	
s^1	W_2		
s^0	$K_t K_f K_I$		

  where

$$W_1 = \frac{(LB_m + J_m R)(RB_m + K_t K_b + K_t K_f K_R) - LJ_m K_t K_f K_P}{LB_m + LEJmR}$$

$$W_2 = \frac{W_1 K_t K_f K_P - (LB_m + J_m R) K_t K_f K_I}{W_1}$$

  According to the Routh-Hurwitz stability criterion, for the system to be stable, the elements of the first column of the Routh array must be of the same sign. From the fact that all motor physical parameters must be positive, the first element LJ_m and the second element $LB_m + J_m R$ are obviously positive. Thus it is left to require that

  $W_1 > 0$, $W_2 > 0$ and $K_t K_f K_I > 0$

  From $W_1 > 0$, we derive

$$(LB_m + J_m R)(RB_m + K_t K_b + K_t K_f K_R) - LJK_t K_f K_P > 0$$

which results in

$$K_P < \frac{(LB_m + J_m R)(RF + K_t K_b + K_t K_f K_R)}{LJ_m K_t K_f} \tag{31}$$

From $W_2 > 0$, we obtain

$$W_1 K_t K_f K_P - (LB_m + J_m R) K_t K_f K_I > 0$$

which results in

$$(LB_m + J_m R)(RB_m + K_t K_b + K_t K_f K_R) K_t K_f K_P > LJ(K_t K_f K_P)^2 + (LB_m + J_m R)^2 K_t K_f K_I \tag{32}$$

Finally from $K_t K_f K_I > 0$, since $K_t > 0$ and $K_f > 0$, it is required that

$$K_I > 0 \tag{33}$$

The inequalities given in Equations (31), (32) and (33) will be used to select K_P, K_I and K_R to ensure the system stability.

- **Case 2: PR Controller**

  The Routh array for the PR controller can be readily obtained by simply setting $K_I = 0$ in the above Routh array that was obtained for the PIR controller. Consequently the Routh Array of $\Delta_3(s)$ is given as follows:

s^3	LJ_m	$RB_m + K_t K_b + K_t K_f K_R$
s^2	$LB_m + J_m R$	$K_t K_f K_P$
s^1	W_1	
s^0	$K_t K_f K_P$	

  Inspecting the above Routh array, in order to ensure the system stability, it is required that $W_1 > 0$ and $K_t K_f K_P > 0$. As in the case of PIR controller, the inequality $W_1 > 0$ yields the inequality given in (31). Furthermore from $K_t K_f K_P > 0$, since $K_T > 0$ and $K_f > 0$, it is also required that

$$K_P > 0 \tag{34}$$

  The inequalities given in Equations (31) and (34) will be used to select K_P and K_R that ensure the system stability.

3.5 Computer Simulation Study

This section reports the results of the computer simulation study conducted to investigate the performance of the ROMPS control system using a simulation software called the System Simulation Language (SYSL) [4].

3.5.1 Motor Parameters

The parameters used in the computer simulation are tabulated below.

Parameters	Units	Elevation	Azimuth	Radial	Gripper
J	$oz \cdot in \cdot sec^2$	4.9×10^{-3}	1.2×10^{-3}	2.67×10^{-5}	1.3×10^{-4}
L	$H(\frac{V\cdot sec}{amp})$	1.8×10^{-3}	1.4×10^{-3}	0.55×10^{-3}	1.2×10^{-3}
F	$\frac{oz\cdot in}{rpm}$	1.7×10^{-3}	3.5×10^{-4}	1.24×10^{-5}	6.9×10^{-5}
F	$\frac{oz\cdot in\cdot sec}{rad}$	1.62×10^{-2}	3.34×10^{-3}	1.1841×10^{-4}	6.589×10^{-4}
R	ohms	2.5	2.9	3.86	3.7
K_b	$\frac{V\cdot sec}{rad}$	0.169	0.0886	0.016	0.034
K_f	$\frac{in}{rad}$	0.01253	0.04377	6.2659×10^{-4}	1.9894×10^{-4}
K_T	$\frac{oz\cdot in}{amp}$	24.0	12.5	2.2	4.8
Max_curr	amp	1.5	1.4	0.45	1.0
Max_spd	$\frac{in}{sec}$	1.7087	11.4675	0.9252	0.135

Table 1: Motor parameters.

In Table 1, Max_curr and Max_spd denote the maximum current and speed, respectively. The calculations of K_f and Max_spd for each study case are given in Appendix A and Appendix B. The maximum voltage, Max_volt used in the computer simulation study is 28 volts.

3.5.2 Trajectory Planner

In the computer simulation, the time trajectories of the desired motor velocity and displacement are generated by a trajectory planner. The subroutine Profile implementing the trajectory planner (Figure 2.10) produces a control position trajectory and a control speed trajectory based upon the targetPosition and the maxSpeed supplied by the user as described as follows. When a "move" command is initiated, Profile subroutine sets the control speed either to +maxSpeed or -maxSpeed depending on the desired direction of motion. It also sets the controlPosition to the current position of the axis. Then on each successive five msec cycle, it adds controlSpeed to controlPosition, causing the controlSpeed to stairstep (ramp) toward targetPosition (Figure 2.11). The Profile subroutine also produces a boolean value which is 0 when the controlPosition is ramping and 1 when the ramping is finished (steady-state). This boolean value serves a switch to turn off (boolean value=0) and on (boolean value=1) the I controller as shown in Figure 2.6.

3.6 Conclusions For Phase II

Phase II has dealt with modeling and control of the ROMPS robot. Four study cases were conducted to study the control performance of the elevation, radial, azimuth axes and the robot gripper in various scenarios. The equations of motion of a permanent magnet DC motor was employed to model the brushless DC motor to be used in actuating the robot axes. Modeling of vibrations along the elevation and radial axes, caused by the robot wrist compliant device was performed using spring-mass models. Load torques generated by the wrist compliant device and the finger compliance mechanism were computed. Using Routh Hurwitz method, stability analysis was conducted for proper selection of the controller gains which ensure the closed-loop system stability. To conclude the discussion of Phase II, we would like to present the following observations and recommendations:

- **Stability Analysis**
  Although a careful stability analysis was conducted for the gain selection ensuring the system stability, we should be aware of the following. System stability implies that the error will decay to zero, but does not control the transient behavior of the responses. Consequently, in order to achieve a desired behavior of the transient response, *cut and try* method should be employed to select the controller gains.

- **Gain Selection**
  Simulation results showed that the same set of PIR gains used for free motion control (Study Case 1) can be used to give satisfactory performance in compliant motion as in Study Cases 2, 3 and 4. Consequently it is not necessary to change the controller gains when going from free motion to compliant motion, and vice versa.

- **Future Simulation Study**
  We learned after working intensively with SYSL that the most time consuming part of the computer simulation study is the coding of the modeling equations, running the resulting programs and debugging it. SYSL is especially sensitive to initial conditions and sampling rates. As a result, we would like to recommend that future computer simulation study be conducted using a simulation package that requires minimal coding such as Matlab/Simulink.

- **Advanced Control Schemes**
  The stability analysis using the Routh Hurwitz method provides a way to select a set of PIR gains which ensure the system stability for a set of parameters and conditions of the motor, robot and environment. The controller gains are fixed and therefore may not provide good performance if the parameters and conditions are changed. We would like to recommend that advanced control schemes such as adaptive control, learning control and fuzzy control, etc. be used for the next generation of ROMPS robot. This type of advanced control schemes are able to adjust their controller gains to effectively adapt to the changes in the system parameters and environment.

References

[1] **Kuo, B.C.**, Automatic Control System, Sixth Edition, Prentice Hall, New Jersey, 1991.

[2] **Nguyen, C.C.**, "Testing of ROMPS Robot Mechanical Interfaces and Compliant Device," *Semiannual Progress Report*, NASA/Goddard Space Flight Center, Grant NAG 5-1415, March 1993.

[3] **Purves, L.**, "Robot Operated Materials Processing System (ROMPS), Critical Design Review (CDR)," NASA/Goddard Space Flight Center, 1992.

[4] **SYSL User's Guides**, System Simulation Language, Version 3, E^2 *Consulting*, California, December 1992.

[5] **Goddard Space Flight Center/NASA**, "Robot Operated Materials Processing System (ROMPS), Phase III, Flight Safety Data Package," *GSFC/NASA*, April 1994.

[6] **Nguyen, C.C.**, "Testing of ROMPS Robot Mechanical Interfaces and Compliant Device," *Semiannual Progress Report*, NASA/Goddard Space Flight Center, Grant NAG 5-1415, March 1993.

[7] **Nguyen, C.C., Antrazi, S., Zhou, Z-L, and Campbell, Jr., C.E.**, "Analysis and Implementation of a 6 DOF Stewart-Platform-Based Robotic Wrist," *Computers and Electrical Engineering: An International Journal*, Vol. 17, Number 3, pp. 191-204, 1991.

[8] **Nguyen, C.C.**, "Testing of Robot Fingers and Dedicated Interfaces," *Final Report*, NASA/Goddard Space Flight Center, April 1991

[9] **Nguyen, C.C.**, "Simulation Study of the ROMPS Robot Control System," *Semiannual Progress Report*, NASA/Goddard Space Flight Center, Grant NAG 5-1415, August 1994.

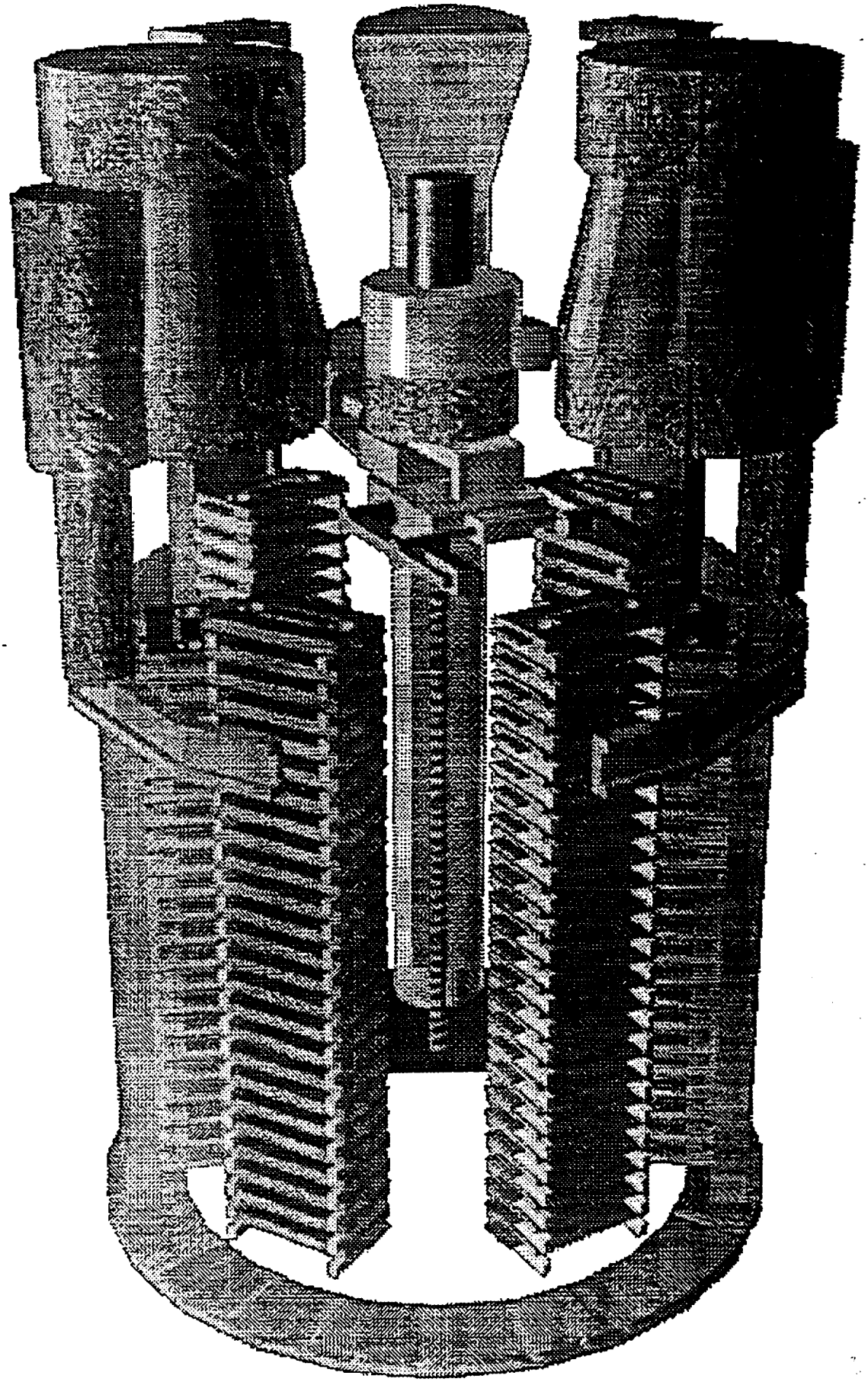

Figure1.1 The Robot Operated Materials Processing System (ROMPS)

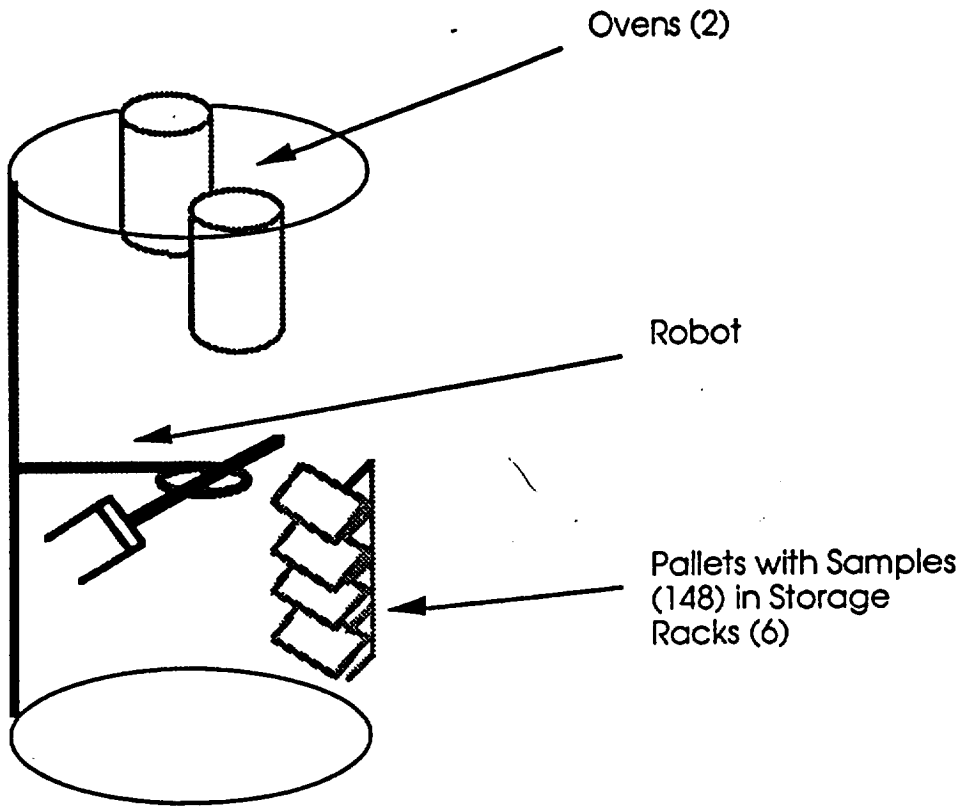

Figure 2 The ROMPS robot

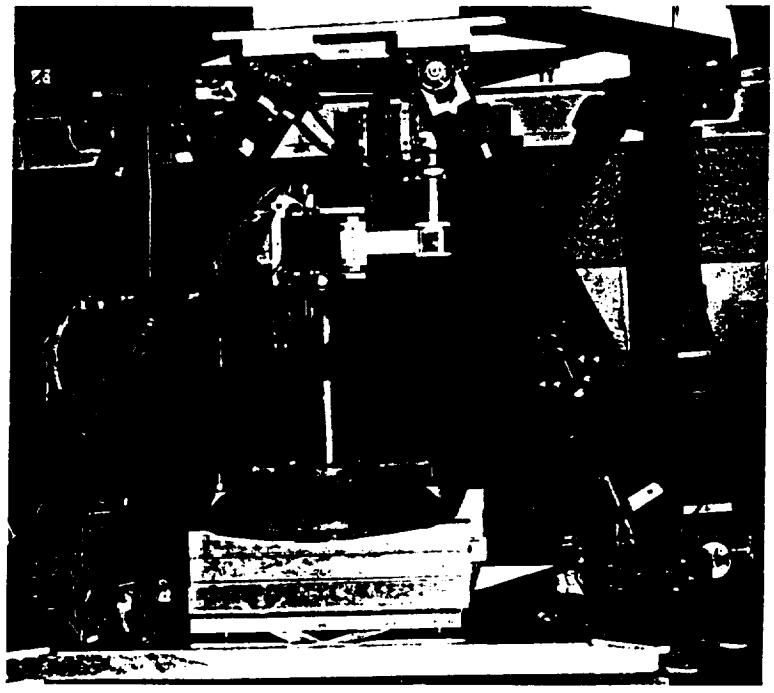

Figure 3 The testbed

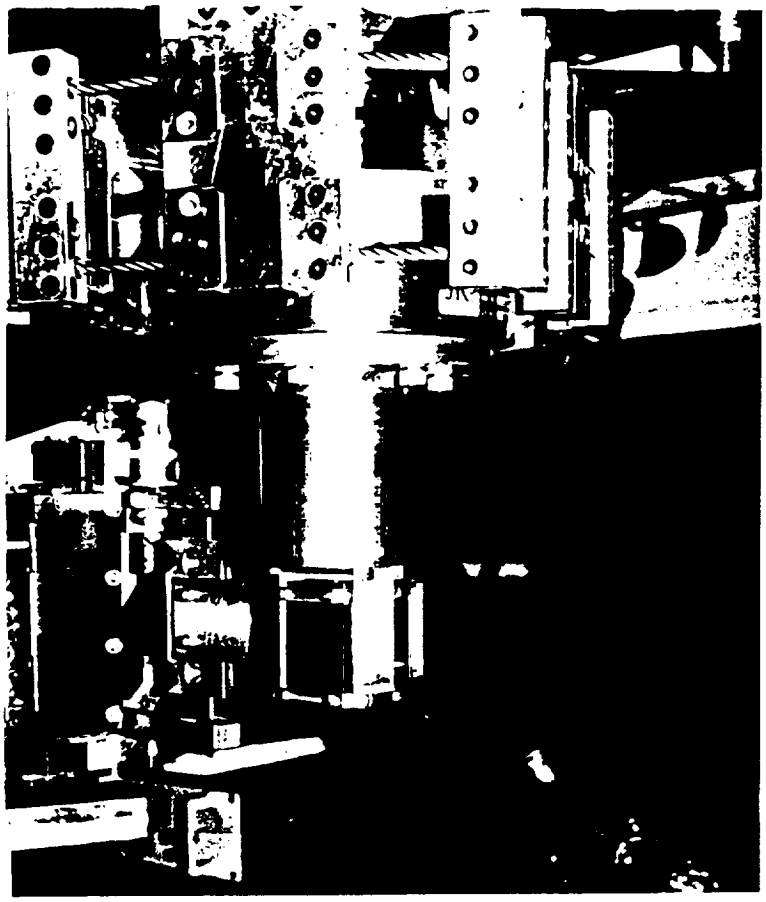

Figure14 The wrist passive compliant device

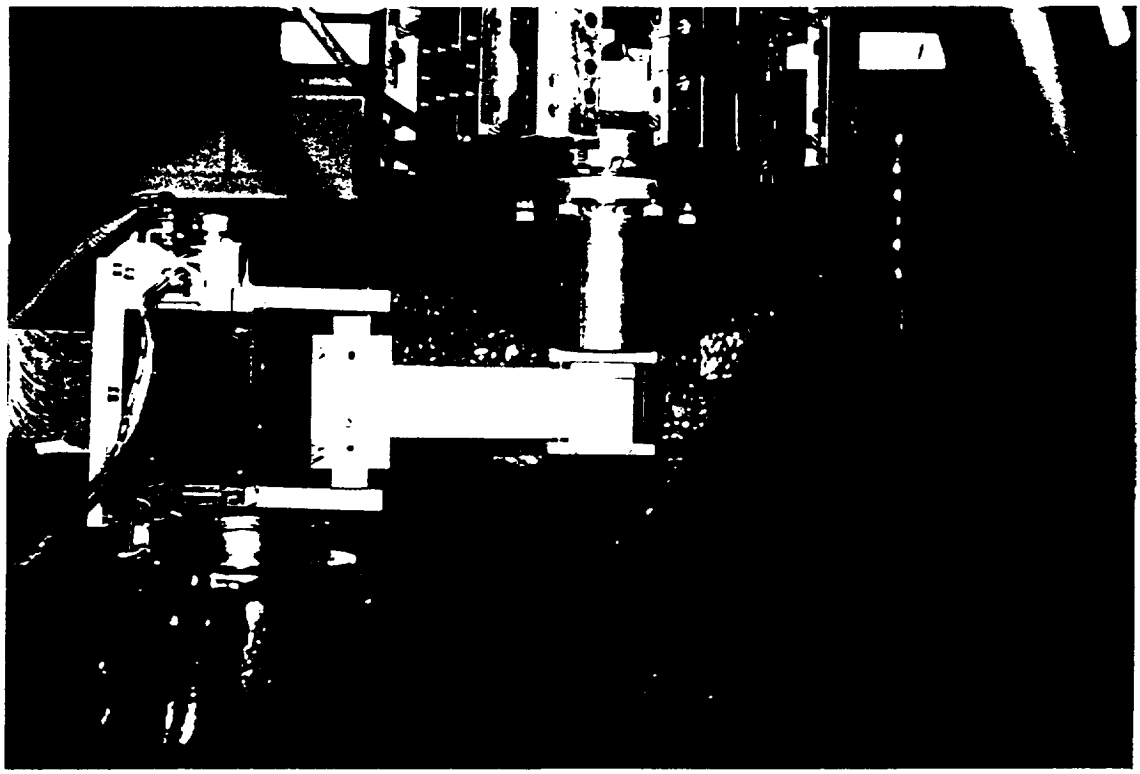

Figure15 Mating test between the pallet and the robot fingers

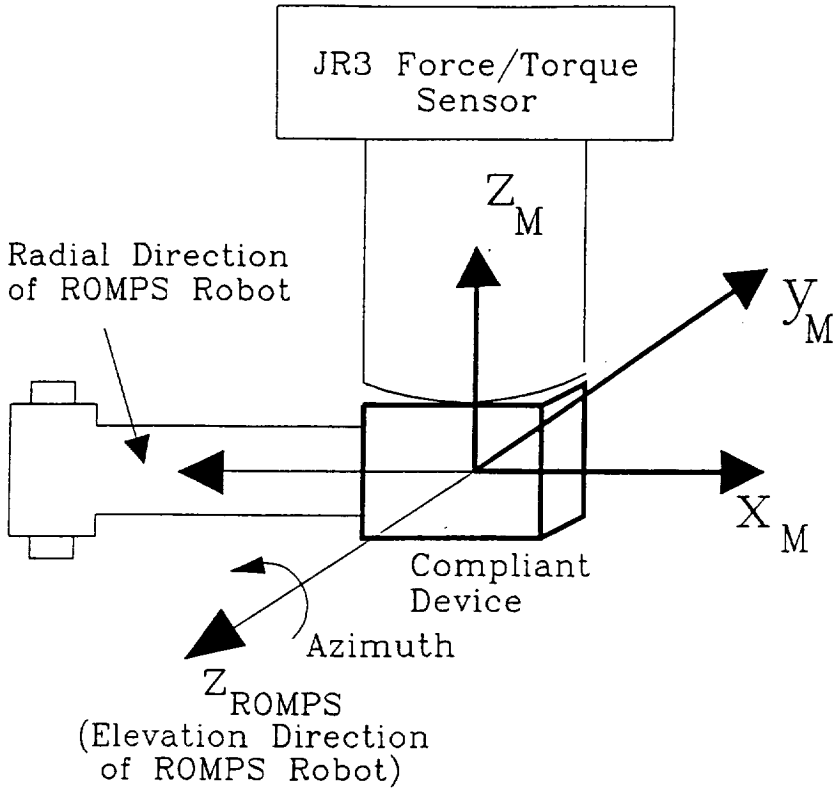

Figure 1.6 Assignment of coordinate systems

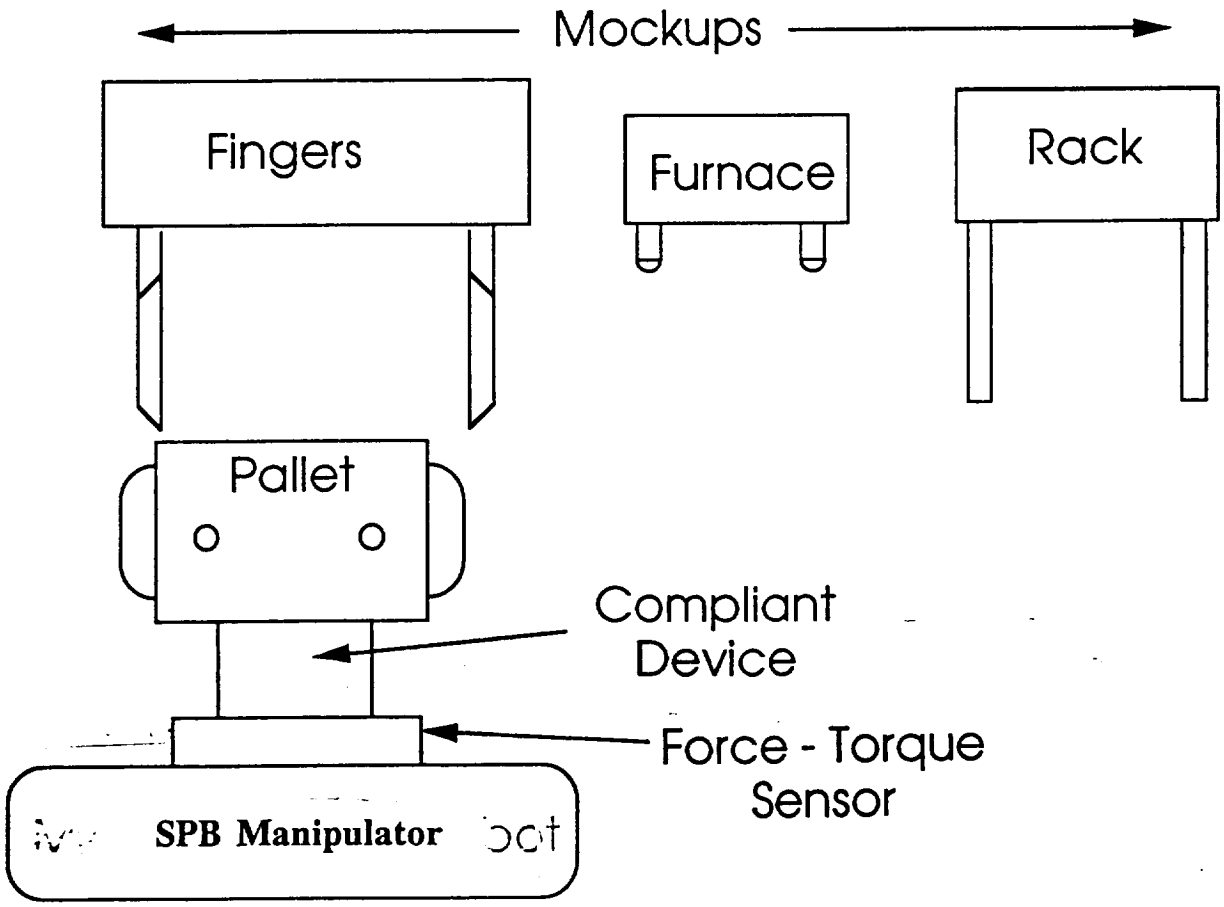

Figure 1.7 The test setup for the three scenarios

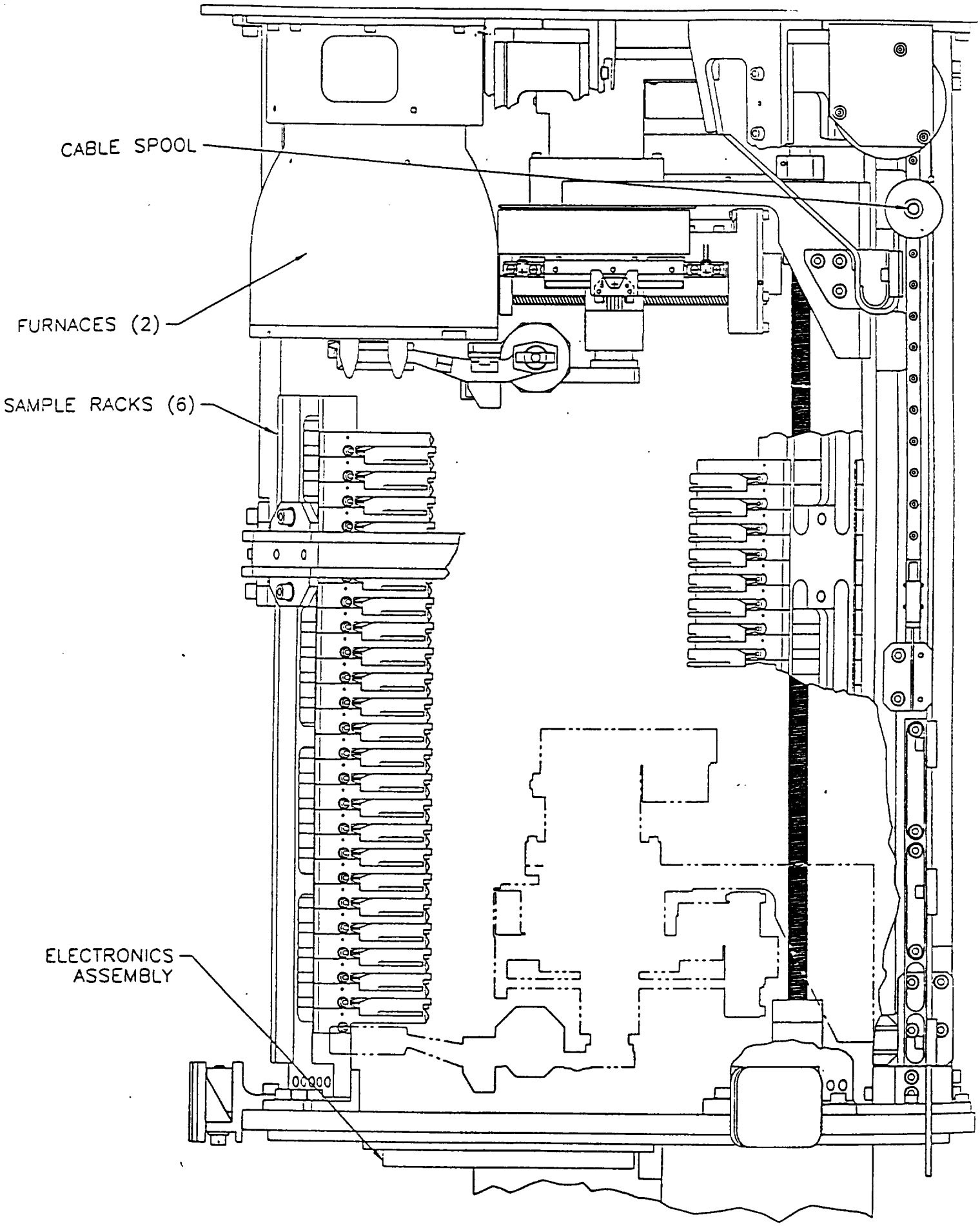

Figure 2.2 Side view of the ROMPS robot

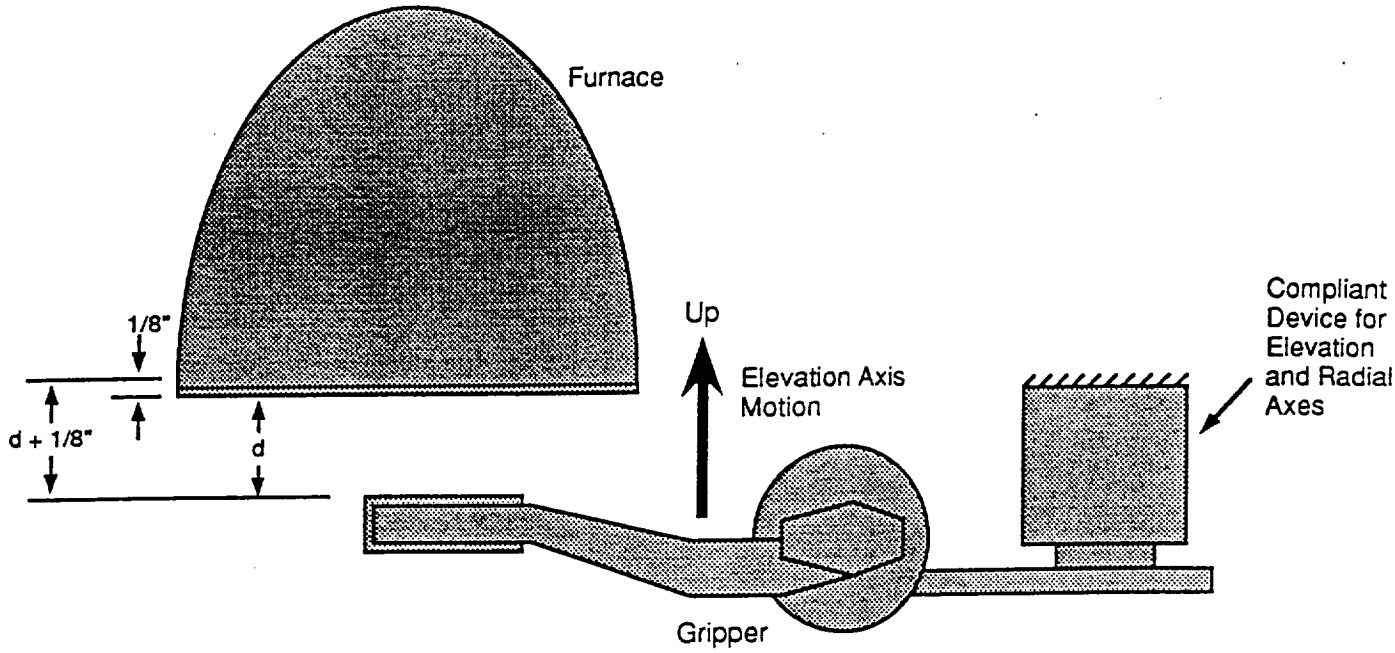

Figure 3 Study of the compliant motion of the elevation axis (Study Case 2)

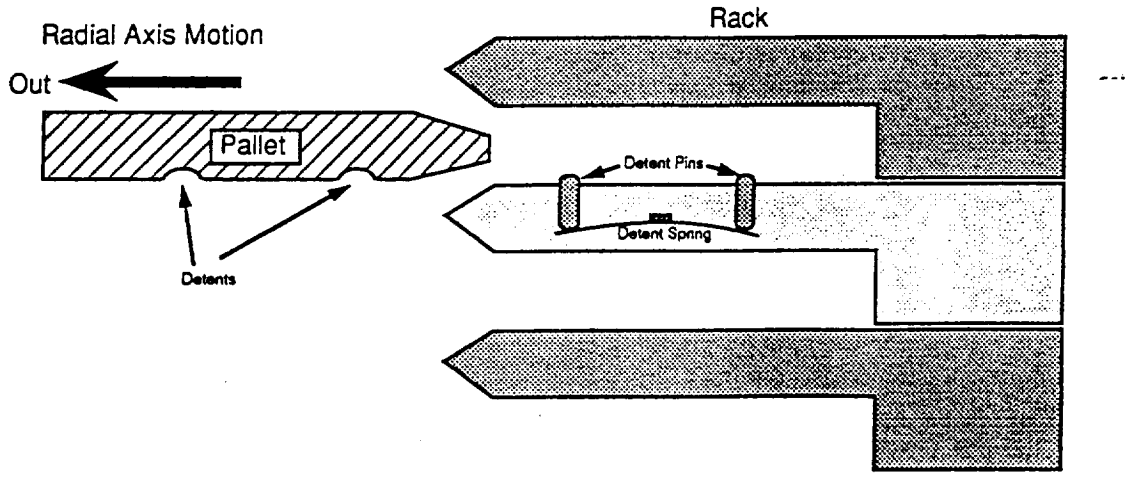

Figure 4 Study of the compliant motion of the radial axis (Study Case 3)

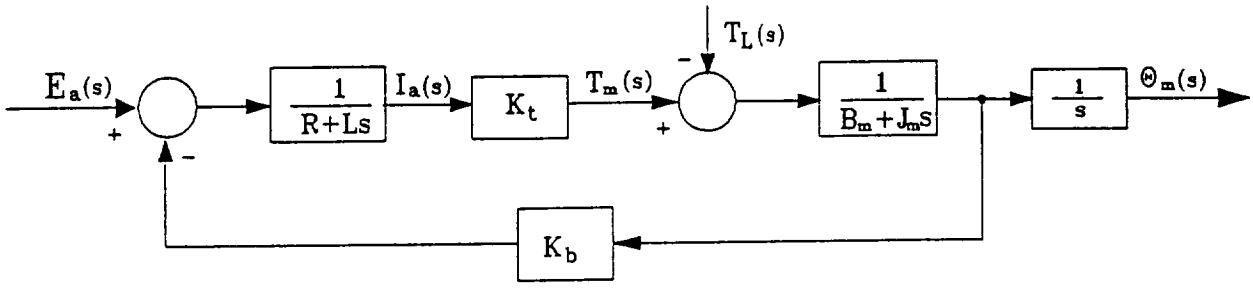

Figure 5 Block diagram of the DC motor

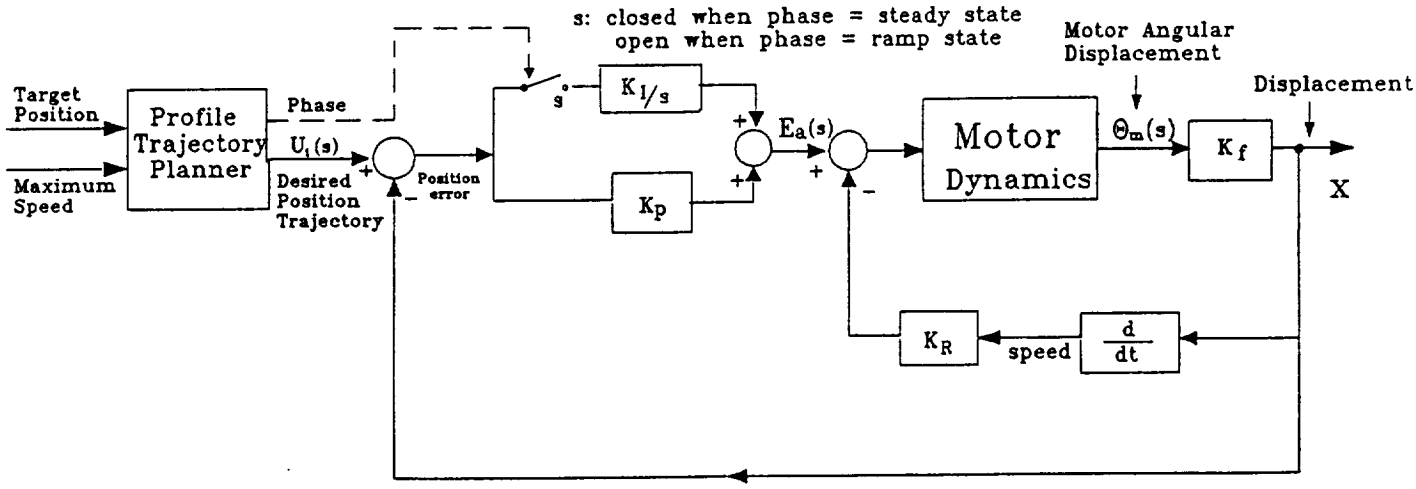

Figure 6 Control system of the brushless DC motor

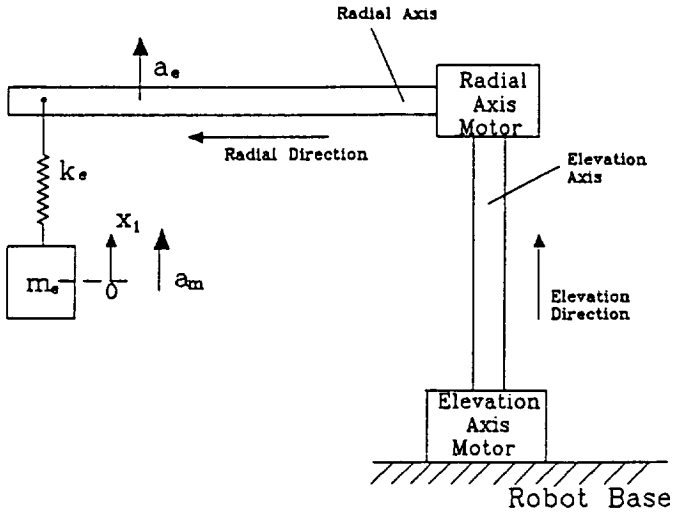

Figure27 Modeling of the vibration along the elevation axis

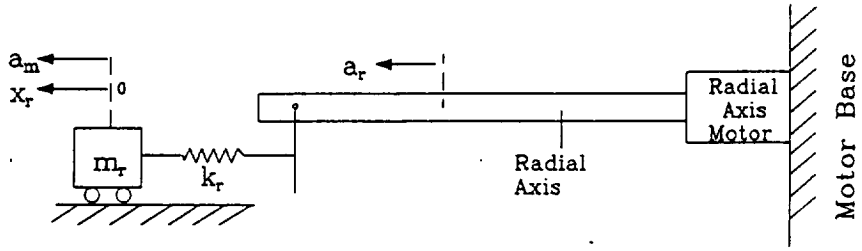

Figure28 Modeling of the vibration along the radial axis

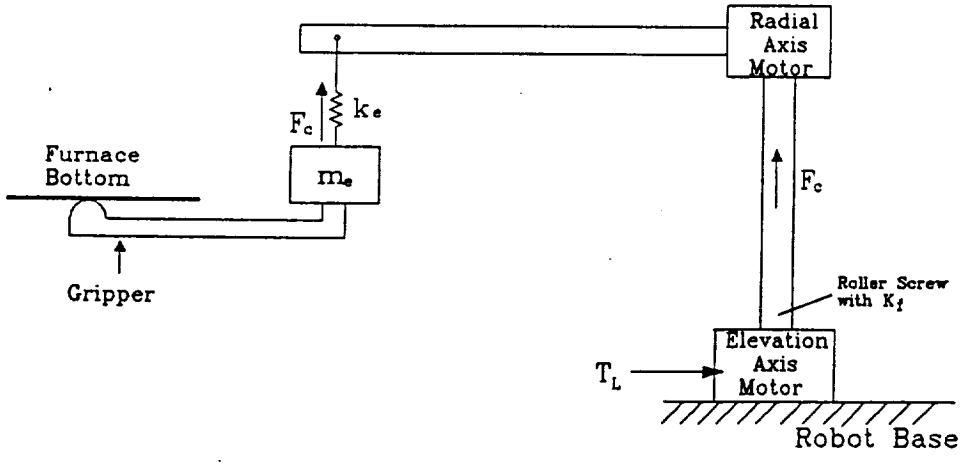

Figure29 Modeling of the motor load torque

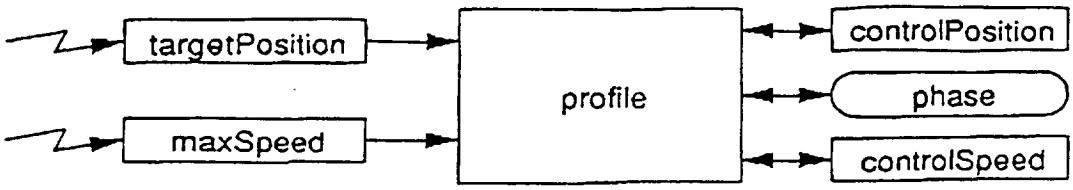

Figure 10 Block diagram of the trajectory planner subroutine (Profile)

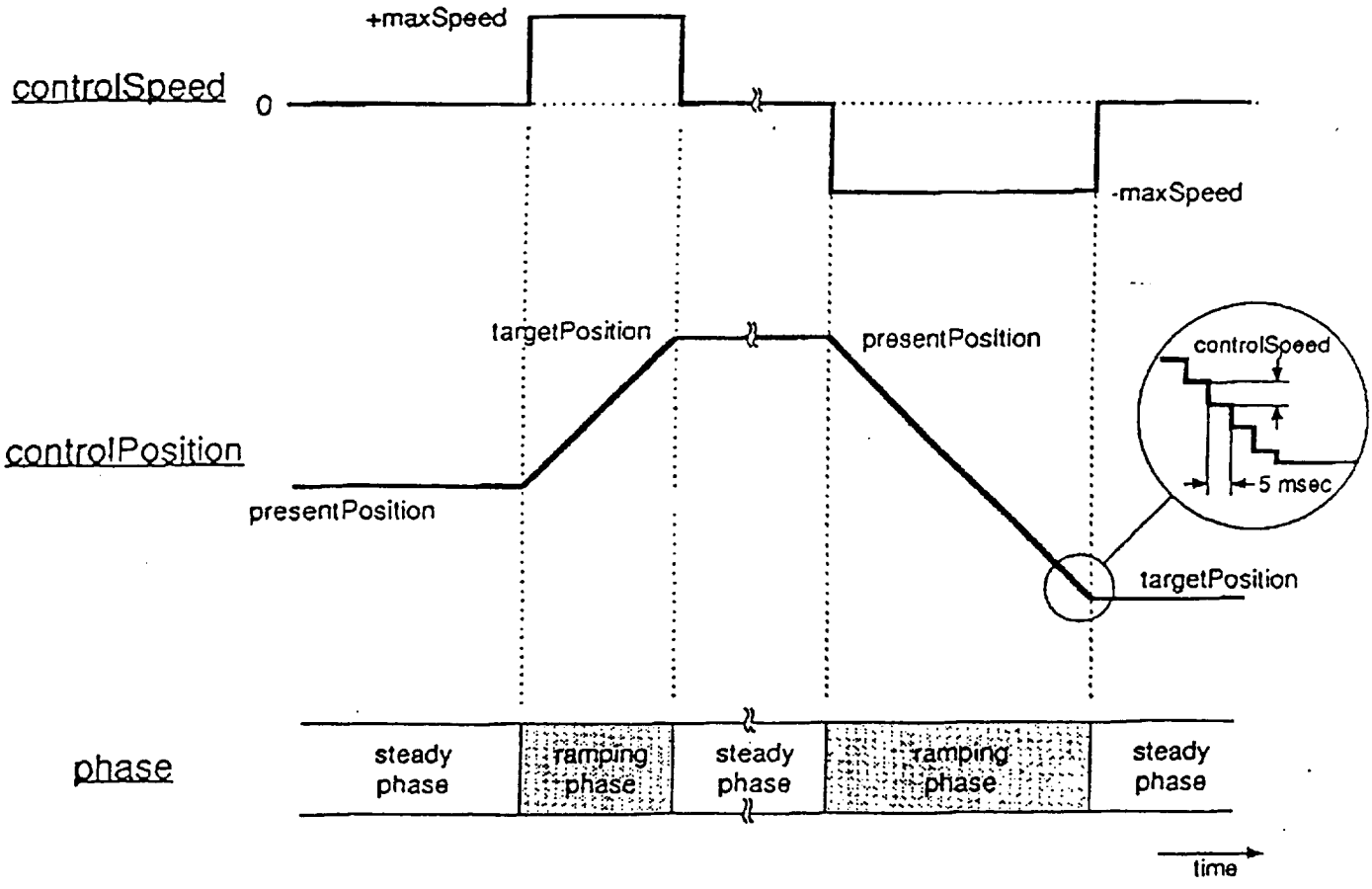

Figure 11 Trajectories of speed and position generated by Profile